NANO EXPRESS **Open Access**

CrossMark

L-Cysteine-Assisted Synthesis of Urchin-Like γ-MnS and Its Lithium Storage Properties

Dan Xu, Ranran Jiao, Yuanwei Sun, Dezhi Sun, Xianxi Zhang, Suyuan Zeng[*] and Youying Di[*]

Abstract

MnS has been attracting more and more attentions in the fields of lithium ion batteries (LIBs) because of its high energy density and low voltage potential. In this paper, we present a simple method for the preparation of urchin-like γ-MnS microstructures using L-cysteine and $MnCl_2 \cdot 4H_2O$ as the starting materials. The urchin-like γ-MnS microstructures exhibit excellent cycling stability (823.4 mA h g^{-1} at a current density of 500 mA g^{-1}, after 1000 cycles). And the discharge voltage is about 0.75 V, making it a good candidate for the application as the anode material in LIBs. SEM, TEM, and XRD were employed to inspect the changes of the active materials during the electrochemical process, which clearly indicate that the structural pulverization and reformation of the γ-MnS microstructures play important roles for the maintenance of the electrochemical performance during the charge/discharge process.

Keywords: Lithium ion battery, Urchin-like γ-MnS microstructures, L-cysteine, Solvothermal

Background

Nowadays, lithium ion batteries (LIBs) have been widely used in our daily lives, such as cellphones, laptops, electric vehicles, and other portable electrical devices [1–4]. Though graphite has been widely used in the commercial LIBs, the relatively low theoretical capacity (372 mA h g^{-1}) and poor rate performance severely limits its application in various fields [5]. Thus, many efforts are devoted to developing electrode materials with high capacity, cycling stability, and low cost.

Recently, transitional metal sulfides such as cobalt sulfides [6–8], nickel sulfides [9, 10], copper sulfides [11, 12], ferric sulfides [13, 14], and manganese sulfides [15–20] have attracted much attention as an alternative for anode material in LIBs. As an important member of transitional metal sulfides, MnS is considered to be a good candidate for the next generation of anode material because of its high energy density (~616 mA h g^{-1}) and low voltage potential (average discharge voltage at ~0.65 V and charge voltage at ~1.25 V) [16, 17, 20, 21]. For this reason, a great number of MnS micro-/nanostructures with different morphologies have been successfully prepared, all of which show excellent electrochemical performance when used as

the anode materials in LIBs. For instance, Robinson and co-workers have successfully prepared MnS nanoparticles using the electrophoretic deposition (EDP) method, which can deliver a reversible capacity of 470 mA h g^{-1} at a current density of C/5 after 100 cycles [12]. Zhang's group has also succeeded in the preparation of coral-like α-MnS using a facile two-step method. Because of the unique structures, the as-synthesized coral-like α-MnS exhibits excellent electrochemical performance. Under a current density of 500 mA g^{-1}, the as-synthesized coral-like α-MnS can still deliver a reversible capacity of 699 mA h g^{-1} after 400 cycles [18]. Kang's group have also reported the synthesis of MnS-C using the spray drying process, which exhibits a discharge capacity of 786 mA h g^{-1} at a current density of 500 mA g^{-1} after 100 cycles [19]. Despite these remarkable progresses, the electrochemical performance of MnS-based anode material is still far from satisfying when considering its practical use in LIBs. According to the previous reports, the relatively poor cycling stability and low discharge capacity are still the main problems that prevent them from large-scale application.

It is well known that the electrochemical performance of the electrode material is highly dependent on its morphology and crystalline texture [5, 6]. Thus, a MnS nanostructure with proper morphological design would be expected to greatly enhance the electrochemical performance of the anode material. Herein, we reported the

* Correspondence: drzengsy@163.com; diyouying@lcu.edu.cn
Shandong Provincial Key Laboratory of Chemical Energy Storage and Novel Cell Technology, School of Chemistry and Chemical Engineering, Liaocheng University, Liaocheng 252059, China

Xu *et al. Nanoscale Research Letters* (2016) 11:444

Page 2 of 10

synthesis of urchin-like γ-MnS via a simple solvothermal method using L-cysteine and $MnCl_2 \cdot 4H_2O$ as the raw materials. Thanks to the unique 3D structure, the as-synthesized urchin-like γ-MnS exhibits excellent cycling stability. The discharge capacity can still reach 823.4 mA h g^{-1} after discharging for 1000 cycles at the current density of 500 mA g^{-1}. Besides the cycling stability, the as-prepared urchin-like γ-MnS structures also exhibit satisfying rate performance. SEM, TEM, and XRD were employed to inspect the changes of the active materials during the electrochemical process, which clearly indicate that the structural pulverization and reformation of the γ-MnS structures play importance roles for the maintenance of the electrochemical performance during the charge/discharge process.

Methods

Preparation of the Urchin-Like γ-MnS Nanostructures

The urchin-like γ-MnS nanostructures were synthesized via a facile solvothermal method. In a typical experiment, 1 mmol $MnCl_2 \cdot 4H_2O$ was firstly dissolved in the mixed solvent composing of 10 mL double-distilled water and 20 mL diethylene glycol (DEG). The mixed solution was then heated to 70 °C under constant stirring. In the next step, 2 mmol L-cysteine was added to the above solution. After heating at 70 °C for 2 h, the white turbid liquid was transferred into a 50-mL Teflon-lined stainless steel autoclave and heated to 180 °C for 18 h. After cooling down to room temperature, the ochre product was collected by centrifugation and washed three times with water and ethanol. The as-obtained product was finally dried in vacuum at 60 °C for 12 h.

Sample Characterizations

Phase purities of the as-prepared samples were characterized using X-ray powder diffraction (XRD, Bruker D8 advanced diffractometer with Cu-Kα radiation, λ = 1.5406 Å). The sizes and morphologies of the samples were investigated using the field emission scanning electron microscopy (FESEM, Hitachi S-4800) and transmission electron microscope (TEM, Hitachi H7700, 120 kV). The high-resolution transmission electron microscopy (HRTEM) images were taken using a transmission electron microscopy (TEM, JEOL-2010) with an accelerating voltage of 200 kV. The surface information as well as chemical composition of the samples were examined using the X-ray photoelectron spectrum (XPS, ESCALAB250). The specific surface area and pore size distribution were determined by the Brunauer-Emmett-Teller (BET) nitrogen adsorption and desorption apparatus (Quantachrome autosorb IQ-C).
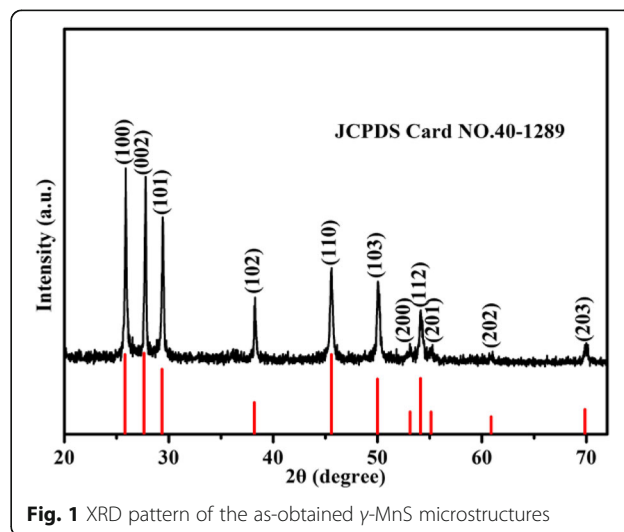
Electrochemical Measurement

The working electrodes were prepared by mixing γ-MnS, carbon black (Super-P) and carboxyl methyl cellulose

binders (CMC) with a weight ratio of 5:3:2. The slurry was coated on copper foil and then dried in vacuum at 100 °C for 12 h. And the active material on each copper foil was weighted to be ~1.46 mg cm^{-2}. The CR2032 coin cells were assembled in an argon-filled glove box (Mikrouna, Super (1220/750)) with moisture and oxygen concentrations below 0.1 ppm. The electrolyte was a solution of 1 M $LiPF_6$ in a mixture of ethylene carbonate (EC), ethyl methyl carbonate (EMC), and diethyl carbonate (DEC) at volume ratio of 4:2:4. Cyclic voltammetry (CV) and electrochemical impedance spectroscopy (EIS) were measured by electrochemical workstation (CHI760E). The galvanostatic charged and discharged characteristics were tested in a voltage range from 0.01 to 3.0 V with LAND CT2001A battery tester.
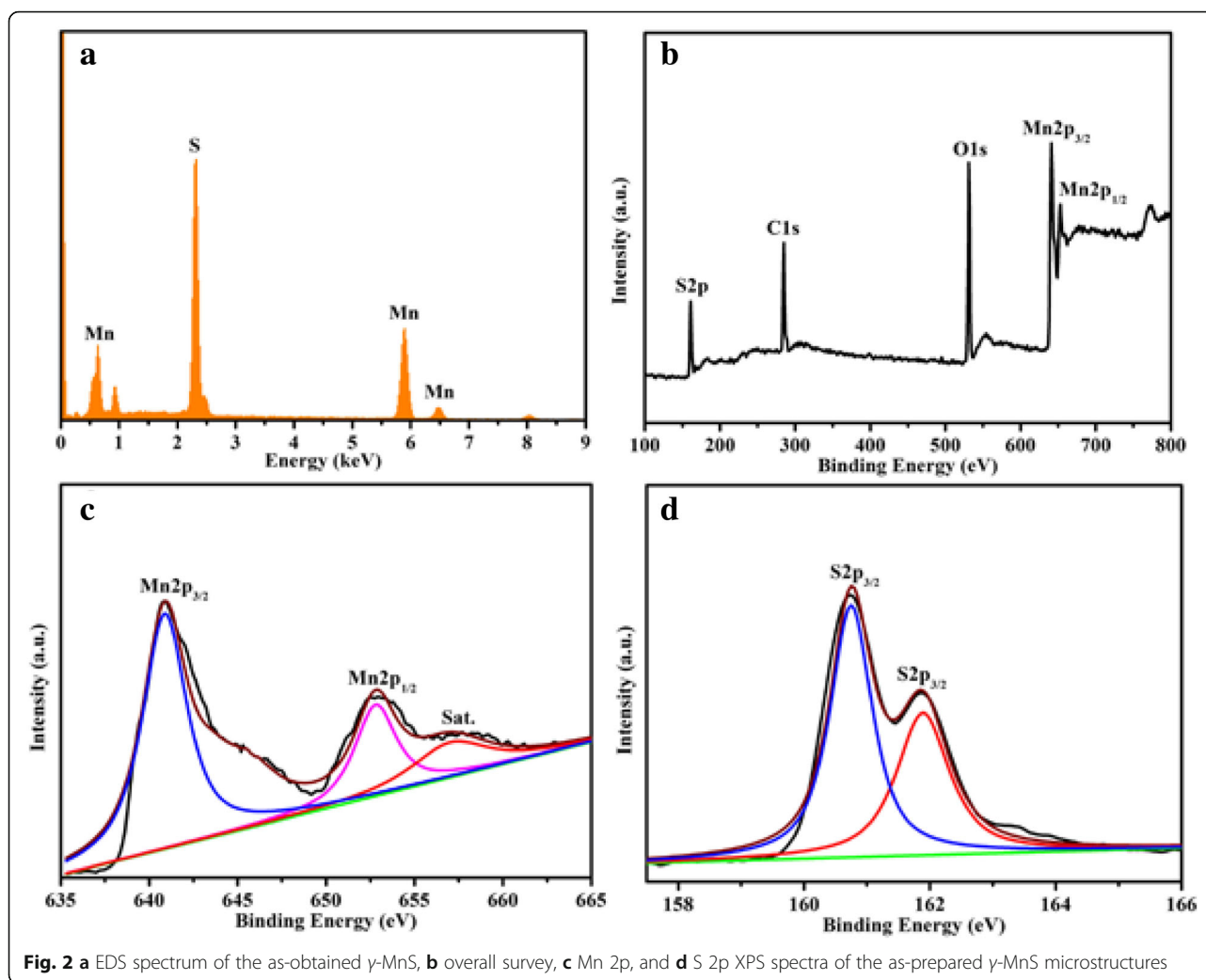
Results and Discussion

The phase purity of the as-prepared product was investigated using the power X-ray diffraction (XRD) and energy-dispersive spectrometer (EDS). Figure 1 is the XRD pattern of the as-synthesized sample, on which all the diffraction peaks can be indexed to be the hexagonal phased γ-MnS. The lattice constants of the as-synthesized sample are calculated to be $a = b = 3.9792$ Å, $c = 6.4469$ Å, $\alpha = \beta = 90.0°$, and $\gamma = 120.0°$, which is consistent with the literature value (JCPDS card no. 40-1289). No other peak is detected, indicating high purity of the as-prepared sample.

The chemical composition of the as-prepared sample is further investigated using X-ray energy-dispersive spectroscopy (EDS), and the corresponding result is shown in Fig. 2a. The corresponding result clearly confirms the existence of elements Mn and S. The atom ratio between Mn and S is determined to be 0.49:0.51, which is in accordance with the theoretical value of MnS. The XPS spectra of the as-synthesized γ-MnS are shown as Fig. 2b–d. The overall

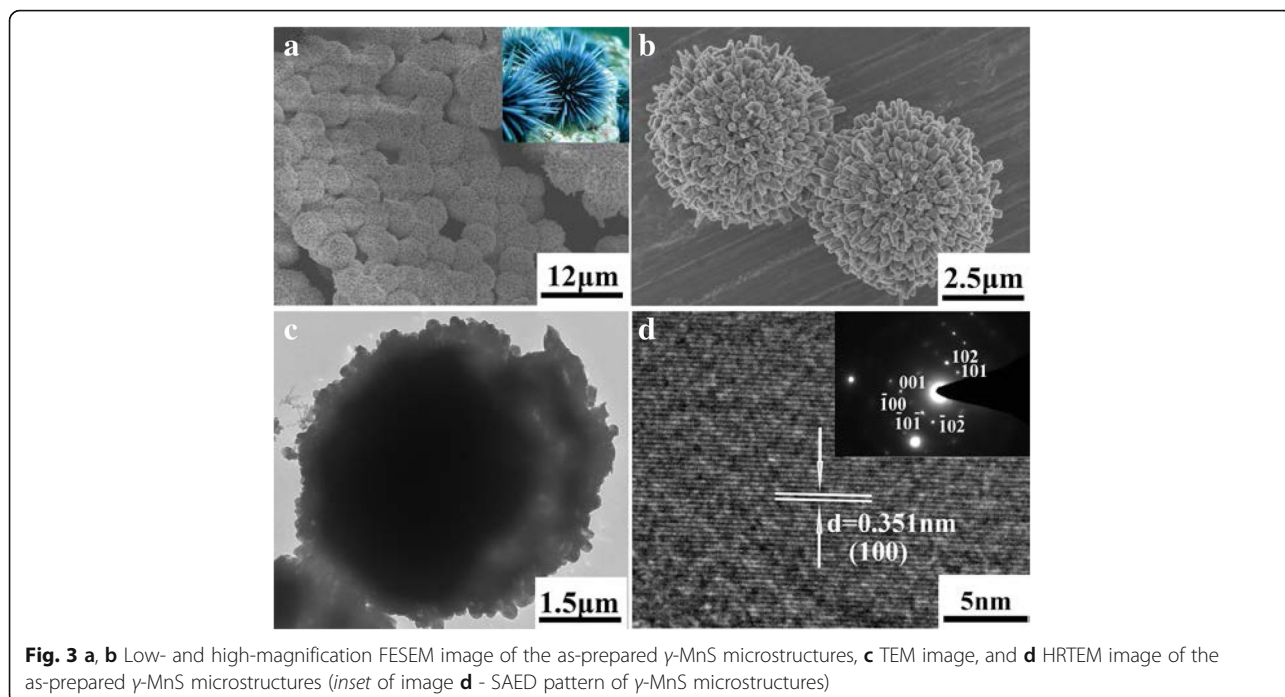**Fig. 1** XRD pattern of the as-obtained γ-MnS microstructures

Xu *et al. Nanoscale Research Letters* (2016) 11:444

Page 3 of 10

Fig. 2 a EDS spectrum of the as-obtained γ-MnS, **b** overall survey, **c** Mn 2p, and **d** S 2p XPS spectra of the as-prepared γ-MnS microstructures

XPS spectrum of the as-synthesized γ-MnS clearly indicates the existence of elements Mn and S (Fig. 2b). The Mn 2p spectrum (Fig. 2c) consists of two peaks with binding energies centering at ~640.8 and ~652.8 eV, which are the characteristic peaks of Mn $2p_{3/2}$ and Mn $2p_{1/2}$, respectively [22]. Similarly, the S 2p spectrum (Fig. 2d) was also composed of two peaks with binding energies of ~160.7 and ~161.9 eV, corresponding to S $2p_{3/2}$ [23]. The XPS results are in well agreement with the XRD and EDS analysis, indicating that the high purity of the as-obtained γ-MnS microstructures.

The morphology and microstructure of the as-synthesized γ-MnS nanostructures were further investigated using FESEM, TEM, and HRTEM. Figure 3a is the low-magnification SEM image of the as-obtained γ-MnS microstructures, which clearly indicate that the as-obtained sample is mainly composed of urchin-like structures. The high-magnification SEM image of the as-prepared sample further indicates that the as-obtained urchin-like structure has a diameter of ca. 5 μm with

acicular crystallites radiating from the center with a uniform size distribution (Fig. 3b). The nanorods grown from the center have uniform diameters of about 150 nm and lengths up to 700 nm. Figure 3c is the TEM image of a single γ-MnS nanostructure, which clearly confirms the urchin-like structure of the as-prepared γ-MnS. To get further insight into the detailed structure of the as-synthesized γ-MnS, SAED and HRTEM were employed. The inset of Fig. 3d is the SAED pattern of γ-MnS, which clearly indicates the single-crystallized nature of the nanorods. Figure 3d is the HRTEM image of a single nanorod from the urchin-like nanostructure, in which clear lattice fringes can be observed. The typical lattice spacing, being determined to be 0.351 nm, corresponds to the (100) lattice plane of hexagonal phased γ-MnS.

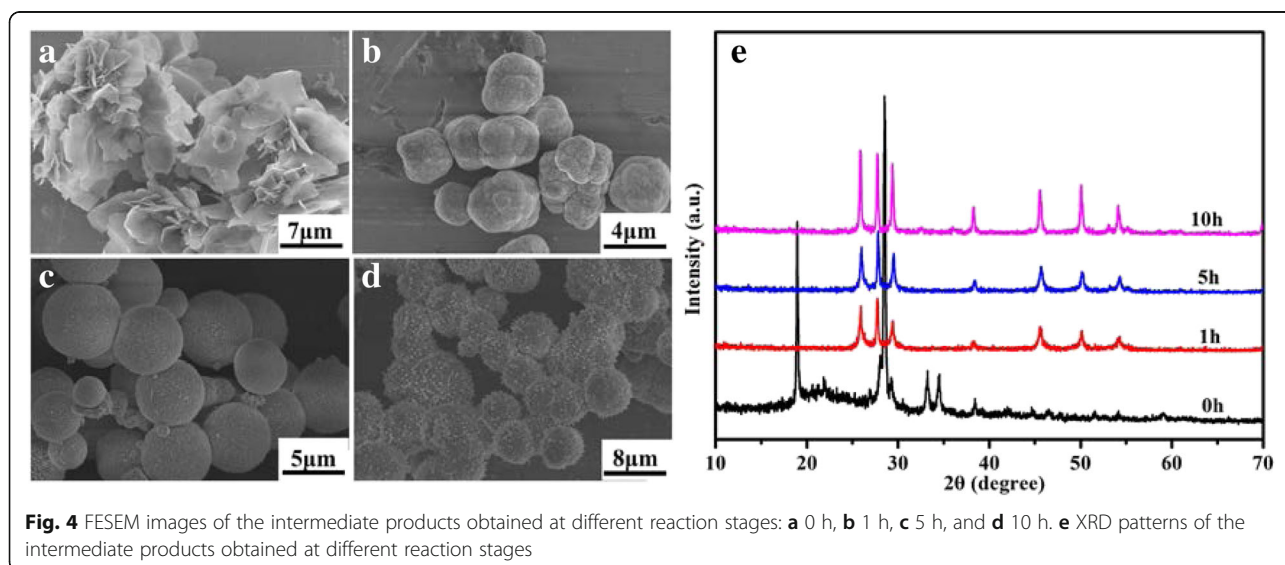To understand the growth mechanism of the urchin-like γ-MnS microstructures, experiments that involved the intermediate products at different reaction times were carried out. Figure 4a is the SEM image of the product obtained after heating at 70 °C for 2 h, which clearly

Xu *et al. Nanoscale Research Letters* (2016) 11:444

Page 4 of 10

Fig. 3 a, **b** Low- and high-magnification FESEM image of the as-prepared γ-MnS microstructures, **c** TEM image, and **d** HRTEM image of the as-prepared γ-MnS microstructures (*inset* of image **d** - SAED pattern of γ-MnS microstructures)
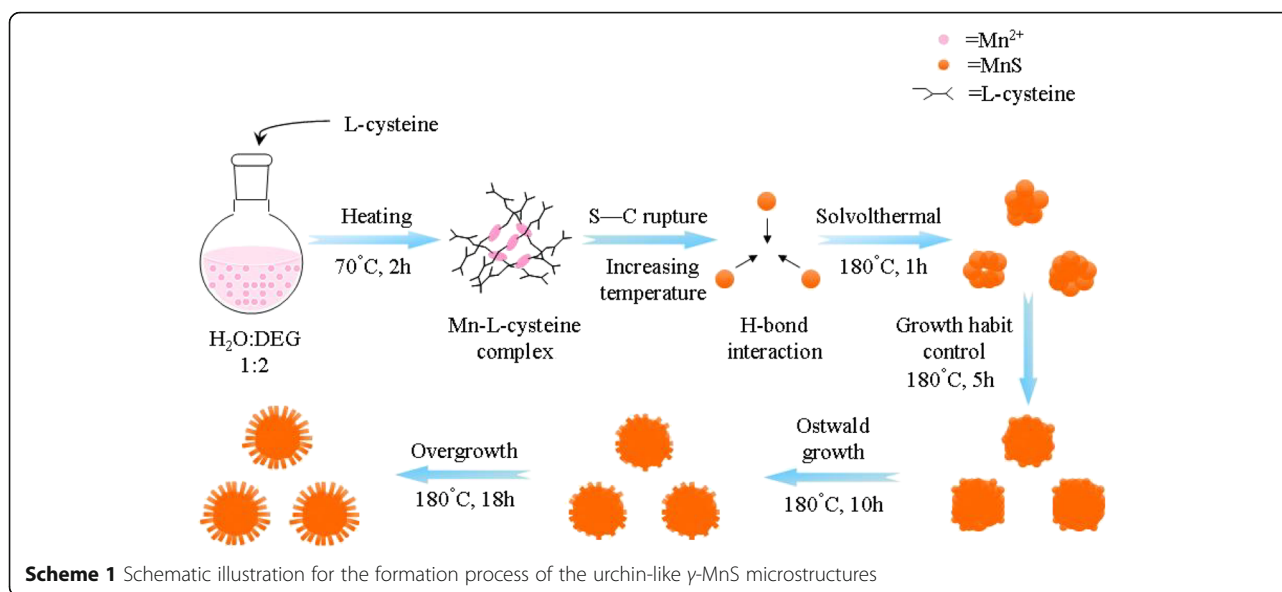
indicates that the sample is composed of a large number of nanoplates. According to the XRD result, these nanoplates can be designated to be the complex that forms between the L-cysteine and Mn^{2+}. As the reaction had been carried out at 180 °C for 1 h, these nanoplates gradually vanished and a large number of irregular microparticles appeared (Fig. 4b). The as-formed irregular microparticles are determined to be γ-MnS, indicating the transformation from Mn-L-cysteine complex to γ-MnS. In the next step, these irregular microparticles gradually transform to γ-MnS microspheres with diameters of about 5 μm (Fig. 4c). A careful observation of these
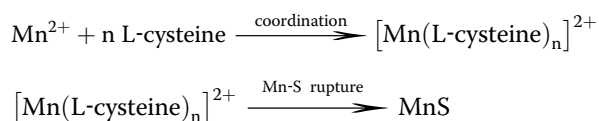
microspheres further indicates that the surfaces of these microspheres are not smooth. A large number of nanoparticles with diameters of about 30 nm can be clearly observed on the surfaces of these microspheres, which will serve as the nuclei centers for the growth of γ-MnS nanorods in the next step. As the reaction went on further, these small nanoparticles will gradually transform to small nanorods. After reacting for 18 h, the urchin-like nanostructure would finally form.

Based on the previous reports and the time-dependent experiments, a two-step formation mechanism for the urchin-like γ-MnS microstructures is proposed (Scheme 1).
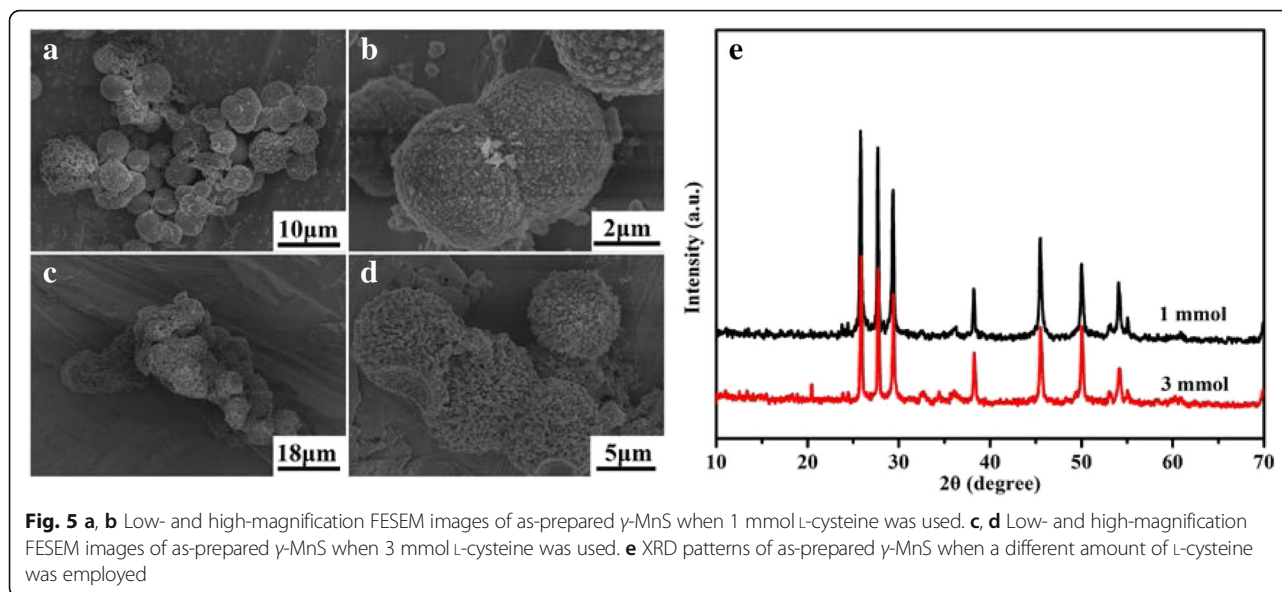

Fig. 4 FESEM images of the intermediate products obtained at different reaction stages: **a** 0 h, **b** 1 h, **c** 5 h, and **d** 10 h. **e** XRD patterns of the intermediate products obtained at different reaction stages

Xu *et al. Nanoscale Research Letters* (2016) 11:444

Page 5 of 10

Scheme 1 Schematic illustration for the formation process of the urchin-like γ-MnS microstructures

Owing to the functional groups in the molecules (–SH, –NH$_2$, and –COOH), L-cysteine molecule is commonly employed for the preparation of metal sulfides with different morphologies [7, 24]. These functional groups usually lead to the versatile role of L-cysteine during the synthetic process, such as sulfur sources, polydentate ligands, self-assembly reagent, or even shape-controlling agent [25–32]. When Mn^{2+} and L-cysteine were mixed in the solvent, a complex between Mn^{2+} and L-cysteine will form, leading to the formation of nanoplates at the initial stage. When the solvothermal reaction began, the initial formed Mn complex will decompose, leading to the formation γ-MnS microparticles. The whole chemical process can be described as

$$Mn^{2+} + n\ L\text{-cysteine} \xrightarrow{\text{coordination}} \left[Mn(L\text{-cysteine})_n\right]^{2+}$$

$$\left[Mn(L\text{-cysteine})_n\right]^{2+} \xrightarrow{\text{Mn-S rupture}} MnS$$

In our synthesis, L-cysteine is excessive. The free thiol groups of the excessive cysteine molecule will bind to the surfaces of the initial formed γ-MnS nanoparticles. Meanwhile, the hydrogen bonds and S-S bonds will form between the cysteine molecules. Driven by the interactions of hydrogen bonds among tiny particles, H$_2$O and DEG, the as-formed γ-MnS tiny nanoparticles will cross-link together, leading to the formation of irregular microparticles when the solvothermal reaction has been conducted for 1 h [7]. As the solvothermal reaction has been conducted at 180 °C for 5 h, these irregular aggregates will gradually transform to γ-MnS microspheres via the Ostwald ripening process [8, 24, 33–36]. Because of the strong interactions between cysteine and Mn^{2+}, the growth rate of γ-MnS can be effectively controlled.

The growth rate in all the direction is nearly the same under the influence of L-cysteine, leading to the formation of γ-MnS microspheres in this step. As the reaction went on, the influence of L-cysteine gradually weakens because of the thermal decomposition process during the solvothermal process. Driven by the intrinsic anisotropic growth habit of γ-MnS, the 1D γ-MnS nanorods will gradually form on the surfaces of the γ-MnS microspheres. As the solvothermal reaction went on, the as-formed nanorods grow longer and longer. When the reaction has been conducted for 18 h, the urchin-like microstructures finally form.

To further investigate the effect of L-cysteine during the synthetic process, comparative experiments employing different amount of L-cysteine were carried out. According to the XRD patterns of the samples when different amount of L-cysteine was employed, the final products under all conditions can be designated to be the hexagonal phased γ-MnS (JCPDS card no. 40-1289). Figure 5a, b are the low- and high-magnification FESEM images of the as-prepared γ-MnS microstructure when 1 mmol L-cysteine was employed, which clearly indicate that the sample is composed of irregular microspheres. Careful observation further indicates that there are some small nanorods on the surfaces of these microspheres. When the amount of L-cysteine increased to 3 mmol, the products are mainly composed of some urchin-like structures as well as some irregular microparticles. As we have mentioned above, L-cysteine not only acts as the sulfur source but also acts as a morphological-controlling agent during the synthetic process. The formation of the complex between Mn and L-cysteine exerts great influence on the formation rate of MnS, which is of vital importance for the morphological control of the final

Xu et al. Nanoscale Research Letters (2016) 11:444

Page 6 of 10

Fig. 5 a, b Low- and high-magnification FESEM images of as-prepared γ-MnS when 1 mmol L-cysteine was used. **c, d** Low- and high-magnification FESEM images of as-prepared γ-MnS when 3 mmol L-cysteine was used. **e** XRD patterns of as-prepared γ-MnS when a different amount of L-cysteine was employed

product. When the concentration of L-cysteine is low, the reaction speed is high, which will result in the formation of the irregular microspheres. When the concentration of L-cysteine is high, the reaction rate becomes low, which would be beneficial for the morphological control of the final product. However, the low reaction rate will also inevitably lead to the incomplete transformation from the irregular microparticles to the urchin-like structures. And this can be used to explain the phenomenon why irregular microparticles as well as urchin-like structures co-exist in the obtained sample when 3 mmol L-cysteine was employed.

As it is shown in Fig. 6, the as-prepared urchin-like γ-MnS exhibits excellent electrochemical performance. Figure 6a shows the cyclic voltammetry (CV) curves between 0 to 3.0 V at a scan rate of 0.1 mV s^{-1}. Two peaks can be observed during the first cycles. The reduction peak centering at 0.49 V can be assigned to the reduction of Mn^{2+} to metallic Mn, while the oxidation peak centering at 1.3 V corresponds to the insertion of Li^+ into the γ-MnS lattice to form a homogeneous phase of Li_2MnS [18, 20, 37, 38]. From the second cycle, the reduction peak shifts from 0.49 to 0.54 V, which could be ascribed to the formation of solid electrolyte interphase (SEI) layer and lithium-driven structural modifications [39–41]. The electrochemical reaction can be summarized by the following equation:
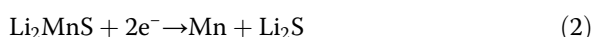
$$MnS + 2Li^+ + 2e^- \rightarrow Li_2MnS \qquad (1)$$

$$Li_2MnS + 2e^- \rightarrow Mn + Li_2S \qquad (2)$$

Figure 6b shows the discharge/charge voltage profiles of the γ-MnS of different cycles at the current of 500 mA g^{-1} between 0.01 and 3.0 V. According to the discharge/charge profiles, the initial discharge capacity is 825.5 mA h g^{-1} and the corresponding columbic efficiency is about 69.06 %. The loss in initial columbic efficiency can be attributed to be the formation of the SEI layer and decomposition of the electrolyte, which have been widely reported for many anode materials [42–45]. The discharge and charge plateaus of the as-prepared γ-MnS electrode are ~0.65 and ~1.25 V, respectively, which are in well agreement with the CV results. The discharging voltage plateau in the second cycle is much higher than the corresponding value in the first cycle, indicating the irreversible reactions of γ-MnS and formation of unstable SEI layer [17, 38, 46, 47]. More interesting, in the third cycle, the discharge and charge plateaus became stable, which is in accord with the cycling performance as shown in Fig. 6c.
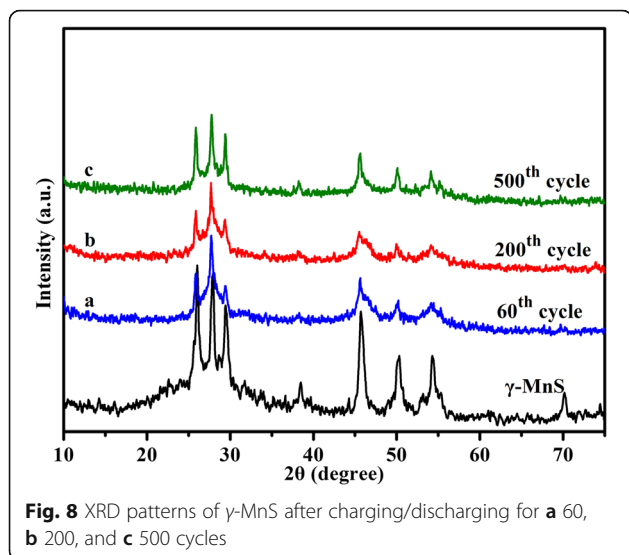
Figure 6c presents the cycling performance of the as-prepared γ-MnS at current density of 500 mA g^{-1}. An obvious decrease in the discharge capacity can be clearly observed in the initial 60 cycles. The discharge capacity of the as-prepared γ-MnS fades significantly in the following cycles, decreasing from 587.8 mA h g^{-1} at second cycle to 379.6 mA h g^{-1} at 60th cycle. This phenomenon could be attributed to the lithiation-induced mechanical degradation and the formation of the unstable SEI layer [47, 48]. To illustrate this view, the coin cell after 60th cycles is disassembled and investigated using FESEM (Fig. 7) and XRD (Fig. 8). According to the XRD pattern, the phase of the active material remains unchanged after the charge/discharge process. However, the urchin-like microstructures disappears and transforms to irregular aggregates. Thus, the pulverization of the active material can be regarded as the main reason for the discharge capacity fading in the initial 60 cycles. After charge/

Xu et al. Nanoscale Research Letters (2016) 11:444

Page 7 of 10
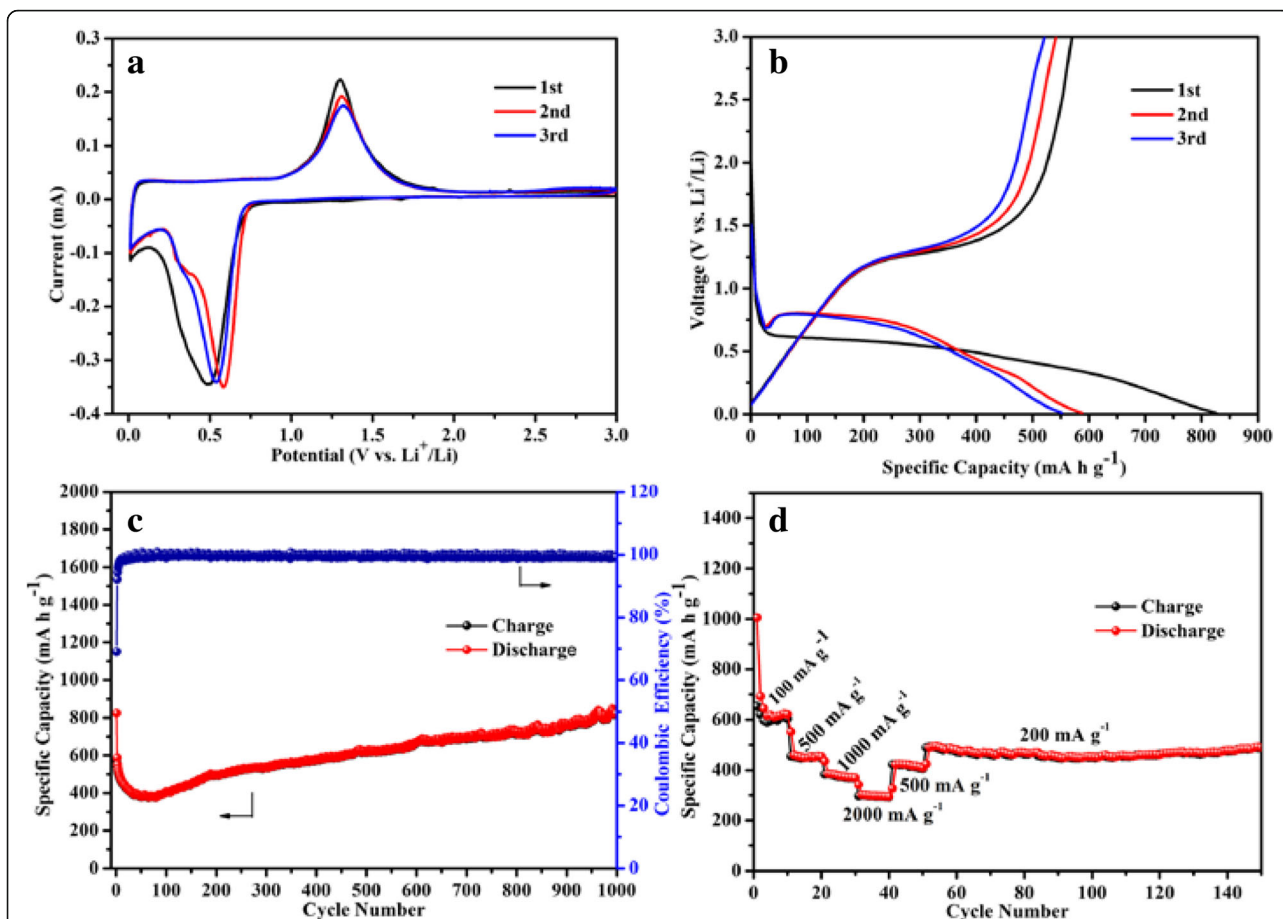
Fig. 6 a CV curves of electrode containing γ-MnS in the voltage range of 0 to 3.0 V, **b** the voltage profiles between 0.01 and 3.00 V at the current density of 500 mA g^{-1}, **c** cycling performance of γ-MnS electrode at current density of 500 mA g^{-1}, and **d** rate performance of electrode containing γ-MnS at different current densities from 100 to 2000 mA g^{-1}
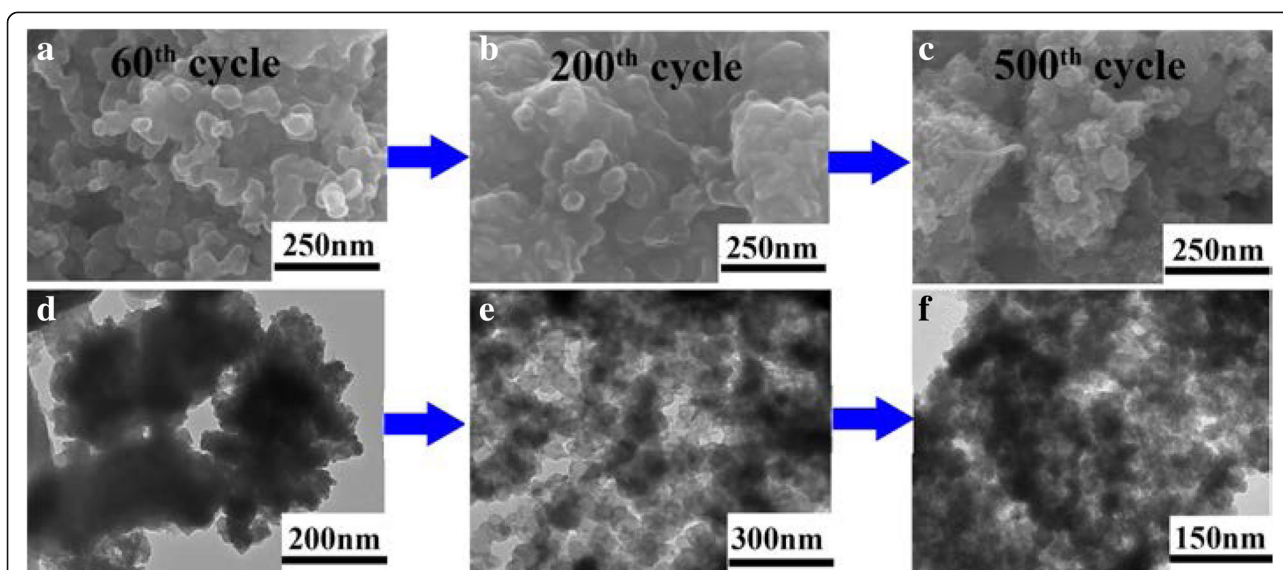
Fig. 7 SEM image evolution of γ-MnS after charge/discharge for **a** 60th, **b** 200th, and **c** 500th cycles. TEM images of γ-MnS after charge/discharge for **d** 60th, **e** 200th, and **f** 500th cycles

Xu *et al. Nanoscale Research Letters* (2016) 11:444

Page 8 of 10

Fig. 8 XRD patterns of γ-MnS after charging/discharging for **a** 60, **b** 200, and **c** 500 cycles

Table 1 Comparison of electrochemical performance with previously reported structure

Material	Current density (mA g^{-1})	Reversible capacity (mA h g^{-1})/cycles	Reference
Urchin-like γ-MnS	500	823.4/1000th	This work
MnS nanoparticles	C/5	470/100th	[12]
γ-MnS/rGO	200	600/100th	[16]
Hollow micro-sphere MnS/RGO	500	830/100th	[17]
Coral-like α-MnS@NC	500	699/400th	[18]
MnS-C	500	636/100th	[19]

discharge for 60 cycles, the discharge capacity gradually increases. To be specific, the discharge capacity increases from 378 mA h g^{-1} at the 60th cycle to 823.4 mA h g^{-1} in the 1000th cycle. It is interesting to note that the discharge capacity after 1000 cycles is higher than the theoretical value of γ-MnS, which may result from the so-called "pseudo-capacitance behavior." This phenomenon is attributed to the reactivated process and stable SEI layer optimization [49, 50]. To get further insight into the capacity decrease in the cycling process, the coin cells after 200th and 500th cycles are also disassembled and investigated using XRD, SEM, and TEM. XRD patterns of the samples clearly indicate that the phase of the active material remains unchanged during the whole charge/discharge process. However, the SEM and TEM observations of the active material clearly indicate the size changes during the charge/discharge process. Upon the increase of the charge/discharge cycles, the active material gradually transforms from irregular microparticles to small nanoparticles. And the size of the active material decreases to 30 and 20 nm upon the 200th and 500th cycle. The size decrease of the active material will provide more active sites for the storage of lithium ions, which is beneficial for the maintenance of electrochemical performance during long cycle. Meanwhile, the irreversible electrochemical reaction during the charge/discharge process will lead to the formation of metallic Mn during the charge/discharge process. The formation of metallic Mn will increase the electrical conductivity of the electrode, which will greatly facilitate the insertion/extraction of lithium ions and transport of electrons, leading to the increment of discharge capacity in the following cycles [43]. What is more, the as-formed metallic Mn could also act as a catalyst for the decomposition of the SEI layer and the reversible formation/dissolution of the organic polymeric film, which would lead to the reversible increase in

the discharge capacity through the so-called "pseudo-capacitance behavior." The anode material is keeping hundreds of cycles without capacity fading, indicating that the mechanical degradation can effectively restructure the active material and optimize SEI layer [47].

Figure 6d presents the rate performance of the urchin-like γ-MnS in LIB applications. Herein, the as-prepared γ-MnS was tested under different charge current densities from 100 to 2000 mA g^{-1}. When the current density is 100 mA g^{-1}, the reversible capacity keeps at ~620 mA h g^{-1} after 10 cycles. When the current density increased to 500, 1000, and 2000 mA g^{-1}, the corresponding reversible capacities are 450, 370, and 300 mA h g^{-1}, respectively. Obviously, the γ-MnS anode material shows excellent performance at a different current density. Even being cycled at 2000 mA g^{-1}, the capacity can still reach 300 mA h g^{-1}. When the current density returns to 200 mA g^{-1}, the capacity of γ-MnS can reach to 490 mA h g^{-1}, which is much higher than that of graphite in the same condition [51, 52]. The rate performance is in accord with the discharge/charge voltage profiles and the cycling performance. A comparison between the reported MnS-based
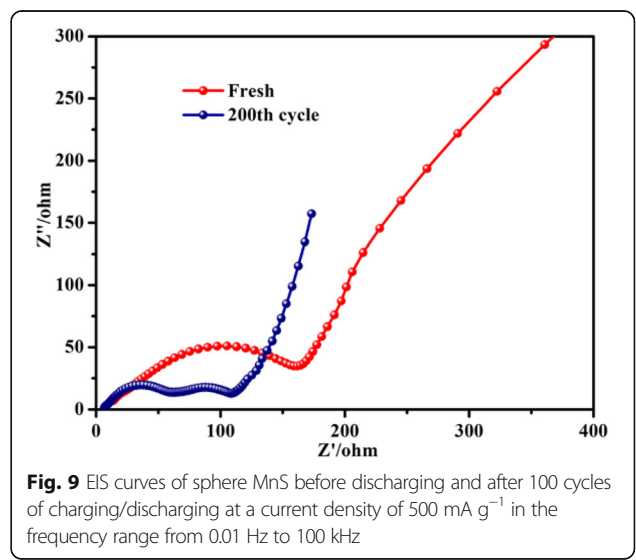
Fig. 9 EIS curves of sphere MnS before discharging and after 100 cycles of charging/discharging at a current density of 500 mA g^{-1} in the frequency range from 0.01 Hz to 100 kHz

Xu et al. Nanoscale Research Letters (2016) 11:444

Page 9 of 10

anode material [12, 16, 18, 19] and our product is summarized in Table 1. Obviously, the as-synthesized γ-MnS in this work shows good electrochemical performance.

To further understand the electrochemical properties of the urchin-like γ-MnS, electrochemical impedance spectroscopy (EIS) was measured at frequencies from 0.01 Hz to 100 kHz and the result is shown as Fig. 9. Nyquist impedance plots indicate that the diameter of the semicircle for sphere-like γ-MnS without charge/discharge process is larger than the corresponding value after 200 cycles, which clearly indicates the formation of the lithium channels and the degradation of the anode material, which is well in accordance with SEM and TEM images at 200th cycle as shown in Fig. 7b, e. In the medium- and high-frequency regions, the single semicircle before the cycles turns into two after 200 cycles, indicating the formation of SEI film.

Conclusions

In summary, urchin-like γ-MnS structures were successfully synthesized by a facile solvothermal method using L-cysteine and $MnCl_2 \cdot 4H_2O$ as the raw materials. A two-step growth mechanism has been proposed for the formation of the urchin-like γ-MnS structures. The product exhibits excellent cycling stability (823.4 mA h g^{-1} at the current density of 500 mA g^{-1} after 1000 cycles) and the discharge voltage is ~0.75 V. SEM, TEM, and XRD were employed to investigate the transformation of the active materials during the charge/discharge process, which clearly indicate that the structural degradation and reformation of the active material play the key roles for the maintenance of the cycling stability. Considering the simple preparation process, excellent cycling stability, and low voltage potential of the as-prepared sample, the product is considered to be a potential candidate anode material in LIBs.

Authors' Contributions
DX prepared the manuscript and carried out the experiment. DZS, XXZ, SYZ, and YYD helped in the technical support for the characterizations. SYZ designed the experiment. RRJ and YWS participated in the experiment. All the authors discussed the results and approved the final manuscript.

Competing Interests
The authors declare that they have no competing interests.

References
1. Mesbahi T, Ouari A, Ghennam T, Berkouk EM, Rizoug N, Mesbahi N, Meradji M (2014) A stand-alone wind power supply with a Li-ion battery energy storage system. Renew Sust Energ Rev 40:204–213
2. Marsh RA, Vukson S, Surampudi S, Ratnakumar BV, Smart MC, Manzo M, Dalton PJ (2001) Li ion batteries for aerospace applications. J Power Sources 97–98:25–27
3. Hu LB, Cui Y (2012) Energy and environmental nanotechnology in conductive paper and textiles. Energy Environ Sci 5:6423–6435
4. Jeong G, Kim YU, Kim H, Kim YJ, Sohn HJ (2011) Prospective materials and applications for Li secondary batteries. Energy Environ Sci 4:1986–2002
5. Liu J, Chen KF, Ji YC, Wan YL, Xue DF, Hodgson P, Li YC (2013) Facile synthesis of transition-metal oxide nanocrystals embedded in hollow carbon microspheres for high-rate lithium-ion-battery anodes. Chem Eur J 19:9811–9816
6. Guo JX, Li FF, Sun YF, Zhang X, Tang L (2015) Graphene-encapsulated cobalt sulfides nanocages with excellent anode performances for lithium ion batteries. Electrochim Acta 167:32–38
7. Liu SG, Mao CP, Niu YB, Yi FL, Hou JK, Lu SY, Jiang J, Xu M, Li CM (2015) Facile synthesis of novel networked ultralong cobalt sulfide nanotubes and its application in supercapacitors. ACS Appl Mater Interfaces 7:25568–25573
8. Bao SJ, Li CM, Guo CX, Qiao (2008) Biomolecule-assisted synthesis of cobalt sulfide nanowires for application in supercapacitors. J Power Sources 180:676–681
9. Lee SM, Ko YN, Choi SH, Kim JH, Kang YC (2015) Capacitive properties of reduced graphene oxide microspheres with uniformly dispersed nickel sulfide nanocrystals prepared by spray pyrolysis. Electrochim Acta 167:287–293
10. Chen QN, Chen WX, Ye JB, Wang Z, Lee JY (2015) L-cysteine-assisted hydrothermal synthesis of nickel disulfide/grapheme composite with enhanced electrochemical performance for eversible lithium storage. J Power Sources 294:51–58
11. Hosseini MR, Schaffie M, Pazouki M, Schippers A, Ranjbar M (2013) A novel electrically enhanced biosynthesis of copper sulfide nanoparticles. Mater Sci Semicond Process 16:250–255
12. Ha DH, Ly T, Caron JM, Zhang HT, Fritz KE, Robinson RD (2015) A general method for high-performance Li-ion battery electrodes from colloidal nanoparticles without the introduction of binders or conductive-carbon additives: the cases of MnS, Cu_{2-x}S and Ge. ACS Appl Mater Interfaces 7: 25053–25060
13. Tran DT, Zhang SS (2015) Chemical stability and electrochemical characteristics of FeS microcrystals as the cathode material of rechargeable lithium batteries. J Mater Chem A 3:12240–12246
14. Wei X, Li WH, Shi JA, Gu L, Yu Y (2015) FeS@C on carbon cloth as flexible electrode for both lithium and sodium storage. ACS Appl Mater Interfaces 7: 27804–27809
15. Li XF, Shen JF, Li N, Ye MX (2015) Fabrication of γ-MnS/rGO composite by facile one-pot solvothermal approach for supercapacitor applications. J Power Sources 282:194–201
16. Ren YR, Wang JW, Huang XB, Ding JN (2015) γ-MnS/reduced graphene oxide nanocomposites with great lithium storage capacity. Solid State Ion 278:138–143
17. Xu XJ, Ji SM, Gu MZ, Liu J (2015) In situ synthesis of MnS hollow microspheres on reduced graphene oxide sheets as high-capacity and long-life anodes for Li- and Na-ion batteries. ACS Appl Mater Interfaces 7: 20957–20964
18. Liu Y, Qiao Y, Zhang WX, Li Z, Hu XL, Yuan LX, Huang YH (2012) Coral-like α-MnS composites with N-doped carbon as anode materials for high-performance lithium-ion batteries. J Mater Chem 22:24026–24033
19. Jeon KM, Cho JS, Kang YC (2015) Electrochemical properties of MnS–C and MnO–C composite powders prepared via spray drying process. J Power Sources 295:9–15
20. Chen DZ, Quan HY, Wang GS, Guo L (2013) Hollow α-MnS spheres and their hybrids with reduced graphene oxide: synthesis, microwave absorption and lithium storage properties. ChemPlusChem 78:843–851
21. Chen DZ, Quan HY, Luo XB, Luo SL (2014) 3-D graphene cross-linked with mesoporous MnS clusters with high lithium storage capability. Scr Mater 76:1–4
22. Xin Y, Cao LY, Huang JF, Liu J, Fei J, Yao CY (2013) Influence of S/Mn molar ratio on the morphology and optical property of γ-MnS thin films prepared by microwave hydrothermal. J Alloys Compd 549:1–5
23. Taleatu BA, Arbab EAA, Mola GT (2015) Stable α-MnS thin film deposited by two-electrode cell: synthesis, structural characterization and photoemission spectroscopic studies. Appl Phys A 120:959–965
24. Zhang B, Ye XC, Hou WY, Zhao Y, Xie Y (2006) Biomolecule-assisted synthesis and electrochemical hydrogen storage of Bi_2S_3 flowerlike patterns with well-aligned nanorods. J Phys Chem B 110:8978–8985

Xu *et al. Nanoscale Research Letters* (2016) 11:444

Page 10 of 10

25. Pan J, Xiong SL, Xi BJ, Li JF, Li JY, Zhou HY, Qian YT (2009) Tartaric acid and L-cysteine synergistic-assisted synthesis of antimony trisulfide hierarchical structures in aqueous solution. Eur J Inorg Chem 35:5302–5306

26. Sandmann A, Kompch A, Mackert V, Liebscher CH, Winterer M (2015) Interaction of L-cysteine with ZnO: structure, surface chemistry and optical properties. Langmuir 31:5701–5711

27. Bao MD, Su HJ, Tan TW (2013) Dark fermentative bio-hydrogen production: effects of substrate pre-treatment and addition of metal ions or L-cysteine. Fuel 112:38–44

28. Thuery P (2011) L-cysteine as a chiral linker in lanthanide–cucurbit[6]uril one-dimensional assemblies. Inorg Chem 50:10558–10560

29. Xiang JH, Cao HQ, Wu QZ, Zhang SC, Zhang XR (2008) L-cysteine-assisted self-assembly of complex PbS structures. Cryst Growth Des 8:3935–3940

30. Zuo F, Yan S, Zhang B, Zhao Y, Xie Y (2008) L-cysteine-assisted synthesis of PbS nanocube-based pagoda-like hierarchical architectures. J Phys Chem C 112:2831–2835

31. Jalilehvand F, Sisombath NS, Schell AC, Facey GA (2015) Lead(II) complex formation with L-cysteine in aqueous solution. Inorg Chem 54:2160–2170

32. Hernández P, Vicente J, Hernández L (2003) Self-assembled monolayer of L-cysteine on a gold electrode as a support for fatty acid, application to the electroanalytical determination of unsaturated fatty acid. Electroanalysis 15:1625–1631

33. Krichevsky O, Stavans J (1993) Correlated Ostwald ripening in two dimensions. J Phys Rev Lett 70:1473–1476

34. Li B, Rong G, Xie Y, Huang L, Feng C (2006) Low-temperature synthesis of α-MnO_2 hollow urchins and their application in rechargeable Li^+ batteries. Inorg Chem 45:6404–6410

35. Ostwald WZ (1897) Studies on formation and transformation of solid materials. Z Phys Chem 22:289–330

36. Bao SJ, Bao QL, Li CM, Chen TP, Sun CQ, Dong ZL, Gan Y, Zhang J (2007) Synthesis and electrical transport of novel channel-structured β-$AgVO_3$. Small 3:1174–1177

37. Yan JM, Huang HZ, Zhang J, Liu ZJ, Yang Y (2005) A study of novel anode material CoS_2 for lithium ion battery. J Power Sources 146:264–269

38. Poizot P, Laruelle S, Grugeon S, Tarascon J-M (2002) Rationalization of the low-potential reactivity of 3D-metal-based inorganic compounds toward Li batteries and energy conversion. J Electrochem Soc 149:A1212–A1217

39. Wang JZ, Du N, Wu H, Zhang H, Yu JX, Yang DR (2013) Order-aligned Mn_3O_4 nanostructures as super high-rate electrodes for rechargeable lithium-ion batteries. J Power Sources 222:32–37

40. Hao Q, Wang JP, Xu CX (2014) Facile preparation of Mn_3O_4 octahedra and their long-term cycle life as an anode material for Li-ion batteries. J Mater Chem A 2:87–93

41. Bai ZC, Fan N, Ju ZC, Guo CL, Qian YT, Tang B, Xiong SL (2013) Facile synthesis of mesoporous Mn_3O_4 nanotubes and their excellent performance for lithium-ion batteries. J Mater Chem A 1:10985–10990

42. Zheng FC, Zhu DQ, Chen QW (2014) Facile fabrication of porous $Ni_xCo_{3-x}O_4$ nanosheets with enhanced electrochemical performance as anode materials for Li-ion batteries. ACS Appl Mater Interfaces 6:9256–9264

43. Zeng PY, Wang XX, Ye M, Ma QY, Li JW, Wang WW, Geng BY, Fang Z (2016) Excellent lithium ion storage property of porous $MnCo_2O_4$ nanorods. RSC Adv 6:23074–23084

44. Ma FX, Wu HB, Xu CY, Zhen L, Lou XW (2015) Self-organized sheaf-like Fe_3O_4/C hierarchical microrods with superior lithium storage properties. Nanoscale 7:4411–4414

45. Yue J, Gu X, Chen L, Wang NN, Jiang XL, Xu HY, Yang J, Qian YT (2014) General synthesis of hollow MnO_2, Mn_3O_4 and MnO nanospheres as superior anode materials for lithium ion batteries. J Mater Chem A 2:17421–17426

46. Bai ZC, Zhang XY, Zhang YW, Guo CL, Tang B (2014) Facile synthesis of mesoporous Mn_3O_4 nanorods as a promising anode material for high performance lithium-ion batteries. J Mater Chem A 2:16755–16760

47. Sun HT, Xin GQ, Hu T, Yu MP, Shao DL, Sun X, Lian J (2014) High-rate lithiation-induced reactivation of mesoporous hollow spheres for long-lived lithium-ion batteries. Nat Commun 5:4526–4533

48. Li WY, Tang YB, Kang WP, Zhang ZY, Yang X, Zhu Y, Zhang WJ, Lee CS (2015) Core–shell Si/C nanospheres embedded in bubble sheet-like carbon film with enhanced performance as lithium ion battery anodes. Small 11:1345–1351

49. Liu LL, An MZ, Yang PX, Zhang JQ (2015) Superior cycle performance and high reversible capacity of SnO_2/grapheme composite as an anode material for lithium-ion batteries. Sci Rep 5:9055–9065

50. Poizot P, Laruelle S, Grugeon S, Dupont L, Tarascon J-M (2000) Nano-sized transition-metal oxides as negative-electrode materials for lithium-ion batteries. Nature 407:496–498

51. Xu JT, Lin Y, Connell JW, Dai LM (2015) Nitrogen-doped holey graphene as an anode for lithium-ion batteries with high volumetric energy density and long cycle life. Small 46:6179–6185

52. Liu XX, Chao DL, Li Y, Hao J, Liu XS, Zhao JP, Lin JY, Fan HJ, Shen ZX (2015) A low-cost and one-step synthesis of N-doped monolithic quasi-graphene films with porous carbon frameworks for Li-ion batteries. Nano Energy 17:43–51